Laser Powder Bed Fusion Processing Of Complex Concentrated Alloys For Bio-Implants

Adrien Mourgout, Amine Hattal, Juliette Gandolfi, Azziz Hocini, Bernardin Mawussi, Lebon Nicolas, Rémy Pirès, Loic Perriere, Guy Dirras

Laser powder bed fusion processing of complex concentrated alloys for bio-implants

A. Mourgout[1] adrien.mourgout@lspm.cnrs.fr; A. Hattal[2] ahattal@z3dlab.com; J. Gandolfi[1] juliette.gandolfi@lspm.cnrs.fr; A. Hocini[1] azziz.hocini@lspm.cnrs.fr; B. Mawussi[3] mawussi@sorbonne-paris-nord.fr; N. Lebon[3] lebon@sorbonne-paris-nord.fr; R. Pirès[4] pires@icmpe.cnrs.fr; Loïc Perrière[4] perriere@icmpe.cnrs.fr; G. Dirras[1] dirras@univ-paris13.fr

1. Université Sorbonne Paris Nord, Laboratoire des Sciences des Procédés et des Matériaux, LSPM, CNRS, UPR 3407, F-93430, Villetaneuse, France,
2. Z3Dlab, Parc Technologique, 26 Rue des Sablons, Montmagny 95360, France
3. Unité de Recherche en Biomatériaux innovants et Interfaces-UR 4462, Université Sorbonne Paris Nord, Bobigny, 93000, France
4. Université Paris-Est Créteil, CNRS, ICMPE (UMR 7182), 2 rue Henri Dunant, 94320, Thiais, France

Abstract

As the population ages in modern societies and the risks of bone diseases or bone accidents increase, there is a need for a new generation of materials with superior biocompatibility and good mechanical properties. This study combines two innovative metallurgical concepts to provide a material solution for the intended application. To this end, multicomponent and complex concentrated alloy (HEA/CCAs) based on TiNbZr-X (X = Mo, Ta) system is fabricated via additive manufacturing (AM), namely by Laser-Powder Bed Fusion (L-PBF) of gas-atomized pre-alloyed powder. After each stage of development by L-PBF through Taguchi's design of experiments, complete microstructure characterization and mechanical behavior of the resulting samples under different loading conditions are conducted. In addition, mechanical surface functionalization carried out by machining with metrological monitoring as a pre-step before a chemical functionalization for the suitability of materials developed for the intended application.

Introduction

The traditional design of metal alloys has always been based on a formulation incorporating solute atoms, in low concentration (minor elements), into a matrix (principal element) via well-known and mastered metallurgy production processes. These processes have resulted in the design of materials with optimized properties for the most prominent applications. However, faced with an increasing demand for materials that must often withstand complex stresses in varied environments, there is a need to propose new material solutions to meet these requirements. Indeed, in the last decade, the new concept of High Entropy Alloy (HEA) introduced in 2004 [1,2] offers a promising opportunity to overcome classic alloy limits. The new alloying concept involves, in most cases, more than five principal elements, each in the concentration range of 5-35 %at. These new multicomponent alloys have resulted so far in improved properties and even performance compared to their conventional counterparts. Indeed, the high number of constituents makes it possible to propose various microstructures and, therefore, a combination of exciting properties for a given system. These materials are made so far by well-known melting processes such as high-frequency electromagnetic induction melting for transition metals [3], vacuum arc melting for refractory components [4], or powder metallurgy based such as the spark plasma sintering [5]. Although multicomponent alloys have been successfully produced using these conventional methods, many challenges remain. For example, the production of parts with complex geometries, and economically sustainable as is the case with biomedical applications. In this case, additive manufacturing (AM) processes can provide an attractive alternative. Indeed, AM processes include an extensive range of versatile techniques for freeform and dense metallic and complex materials. In these processes, a laser or an electron beam is used to melt powders and/or wires to create a "molten pool" in which several complex thermodynamical phenomena occur. In addition, the high-cooling rate of these processes could lead to undesirable microstructural and mechanical properties.

Therefore, a post-heat treatment is sometimes mandatory to achieve high-quality parts. Among AM processes, the ASTM F42 technical committee divides AM processes into seven technologies.

However, only three of them are extensively commercialized today, namely Laser-Powder Bed Fusion (L-PBF) which uses photon or electron-based-laser sources, and Directed Energy Deposition (DED) which could use both laser sources [6]. AM production of refractory multicomponent high entropy alloys (RHEA), which contain high melting point elements, is scarce. Indeed, few studies have shown promising results [7, 8]. Nakano et *al*. used a L-PBF-based process to develop a quinary non-equiatomic $Ti_{1.4}$ $Nb_{0.6}$ $Ta_{0.6}$ $Zr_{1.4}$ $Mo_{0.6}$ RHEA from pre-alloyed powders for biomedical applications, which exhibited excellent biocompatibility, along with enhanced mechanical properties with a 0.2 % proof stress of 1690 MPa higher than the as-cast counterpart [7]. Nevertheless, a transparent step-by-step approach to microstructure optimization considering the influence of the L-PBF processing parameters is still needed.

In this paper, we propose an approach to optimize the microstructure of RHEA, via the implementation of a Taguchi-type experimental plan, from a pre-alloyed powder of composition $Ti_{1.4}NbZrMo_{0.3}Ta_{0.3}$. After analyzing the microstructure resulting from the L-PBF process, the mechanical properties in uniaxial compression are studied. The significant challenges for medical implants manufacturing, are related to the respect of functional requirements, particularly in the assembly areas with the implant abutments and the body part for osteo-integration. Roughness is one of the most important factor impacting these functional requirements. The milling process, for instance, has a significant influence on roughness parameters. Therefore, this paper also evaluates the printed specimens' machinability and the impact of the finishing milling parameters on their roughness.

Materials and Methods

A rod of $Ti_{1.4}NbZrMo_{0.3}Ta_{0.3}$ alloy was fabricated as a starting material and gas-atomized to produce spherical powders (Figure 1) in a range size of 10-63 µm (average size of 30 µm). Taniobis-GmBH processed both the rod and the powder. The L-PBF process was carried out with an SLM 125HL equipment at Z3DLAB SAS company. Table 1 summarizes the L-PBF parameter used to fabricate the bulk alloy parts from a constant layer thickness equal to 30 µm. The reason for selecting these two sets of L-PBF parameters (S1 and S2) is to investigate the effect of low and high Volumetric Energy Density (VED) on the final microstructure of the fabricated parts. Both cube-shaped 5 mm $\times$ 5 mm $\times$ 7 mm) and cylinder-shaped (5 mm x 7 mm) samples were fabricated for microstructure and mechanical characterization. After L-PBF processing, the mass density was measured with a He-gas pycnometer (Micromeritics AccuPyc II 1340). For microstructure investigation, specimens have been cut from the bulk parts and prepared via conventional mechanical polishing steps to obtain Z and X planes (perpendicular and parallel to the building direction, respectively). Microstructure investigations were carried out with a scanning electron microscope (SEM) ZEISS Supra 40VP equipped with Electron Back Scattered Diffraction (EBSD) detector. Phase identification was achieved by X-ray diffraction (XRD) Intel equinox 1000 with Cu source λ (Kα1) = 0.154 nm. Chemical analysis has been done with Energy Dispersive X-ray (EDX) coupled with an SEM Leica S440. For the mechanical properties, compressive tests were conducted at various strain rates in the range 10^{-2} to 10^{-4} s^{-1} using an MTS 20 m. The compression axis was either parallel or perpendicular to the L-PBF building direction, respectively, to investigate the impact of the as-built microstructure heterogeneity on the mechanical properties.

Table 1. L-PBF processing parameters (extracted from Taguchi plan)

Sample	laser power (W)	scan speed (mm/s)	hatching (µm)	Density (g/cm^3)	VED (J/mm^3)
S1	170	800	80	7.389	88.54
S2	200	200	80	7.347	416.67

Machinability experimentations were carried out on $10\times10\times10$ mm^3 cubes. The surfaces of each specimen were milled with a 4-axis industrial CNC (Computer Numerical Control) machine tool (X, Y, Z, A) (DMG 635V Ecoline). The CNC was fitted with two solid carbide end mills referenced HAM 40-1491. Two tool diameters of 6 mm and 8 mm were chosen. Then, roughness parameters were measured with an optical device. To this end, two faces of each specimen were milled. The first face is perpendicular to Z (plane XY), and the second face is parallel to Z (plane XZ). All the milling

experiments were performed in end milling. During the experiments, two jets of lubricant placed on either side of the spindle and directed towards the tool's tip were applied with a constant flow rate. The other machining parameters were fixed and set according to the machining conditions used in the literature [9,10] (Table 2).

Table 2. Milling parameters

Tools	Ø6 mm	Ø8 mm
Cutting speeds	30 m/min	20 m/min
Feed rates	0.05 mm/min	0.025 mm/min
Radial step (ar)	3 mm max	4 mm max
Depth of cut (ap)	0.2 mm	

After milling, each milled surface topography is recorded with a focal variation device (Bruker Alicona, Infinite Focus G5+) [11,12]. The experiments were carried out with an x50 lens and a vertical resolution of 50 nm. Six 2D and 3D roughness parameters were selected according to their ability to characterize the expected functional requirements of the surface. In industrial/mechanical parts applications, the Ra parameter represents 90 % of the expected functionalities, and it is widely used. In addition, two roughness parameters sensitive to peaks and valleys and especially to extreme values are retained: Rt and Rz. In industrial/mechanical parts applications, they represent 80 % of the expected functionalities. The parameters Sa and Sz counterparts of Ra and Rz, respectively, are chosen to characterize the peaks and valleys in 3D. Finally, the surface hybrid parameter Sdr is well adapted to specify osseointegration. For each 3D roughness parameter, a flat surface (approximately 1.7 x 0.31 mm²) per sample surface is recorded. The Lc filter value was set to 800 µm. For each 2D roughness parameter, a profile perpendicular to the printing slices was extracted from the 3D topography. The Lc filter value was also set to 800 µm.

Results and discussion:

Starting powder characteristics

Figure 1 shows a SEM image of the atomized powder along with EDX maps of the chemical elements. EDX analysis shows quite an overall elemental homogeneity in the powder. The mass density yielded an average mass density value equal to 7.389 g/cm^3. Figure 2 shows XRD diffractograms of the powder and both samples. It reveals the presence of BCC structures with wide and split peaks probably due to a slight variability in lattice parameters.

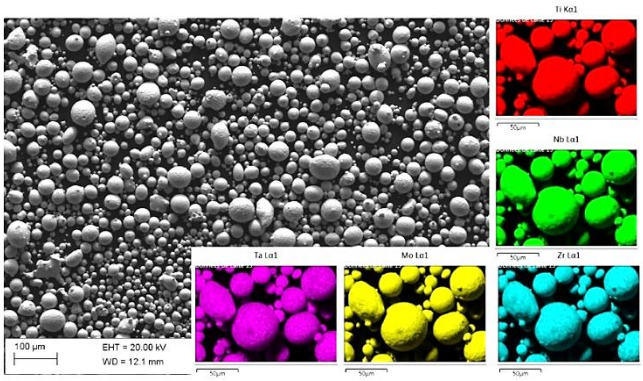

Figure 1. SEM image and EDX maps of elemental elements of the as-received powder

As-built bulk samples

The mass density of samples S1 and S2 (see Table 1) was found to be 7.375 g.cm^{-3} and 7.346 g.cm^{-3}, respectively. These values are slightly lower than for the powder. This must be mainly related to defects resulting from L-PBFed build parts (lack of fusion, balling, …). XRD diffractograms of bulk samples, as shown in Figure 2, have been indexed as BCC structures. For S1, only the (110) peak is a doublet, while S2 shows perfect single peaks; these results show a better homogeneity within the solid solution than the initial pre-alloyed powder.

Moreover, S1 and S2 diffractograms seem to be slightly shifting toward small angles (compared to the powder), meaning an increase in the inter-planar spacing, resulting in the reduction of lattice parameters according to the Bragg formula. In addition, fine peaks are noticed within S1 and S2

(much more pronounced in S2 than in S1). The L-PBF process resulted in a fine microstructure with a small crystallite size [13].

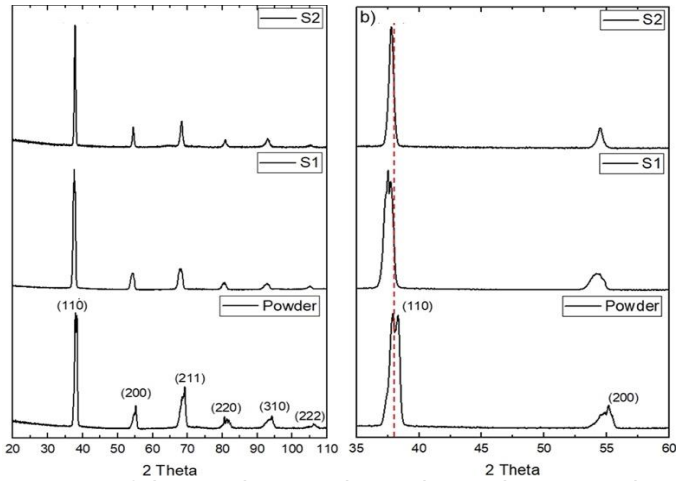

Figure 2. a) XRD diffractogram of the starting powder and samples S1, and S2 (see Table 1). b) a zoom over the peaks of (110) and (110).

Figure 3 illustrates the microstructure (SEM and EBSD) of the polished as-built samples based on the L-PBF parameters of Table 1. S1 sample presents some lack of fusion and several micro-cracks (2 µm width) (Figure 3b). The S2 sample, however, shows no lack of fusion defects but many wide cracks in the center (12 µm wide) (Figure 3c). Therefore, to investigate the possibility of reducing these microstructural defects, cylinder-shaped S1 and S2 samples were fabricated. However, for the same L-PBF parameters (Table 1), micro-cracks and lack of fusion still occurred, which balances out the geometrical effect on cracks formation. A compromise in terms of VED needs to be found to minimize these defects. These cracks appear in both cases mainly related to particle segregation within dendrites and the L-PBF process's high-cooling rate [14]. Examination of the IPF maps showed that the S2 sample displays a more random crystallographic texture compared to S1 one, for which an [001] orientation dominates.

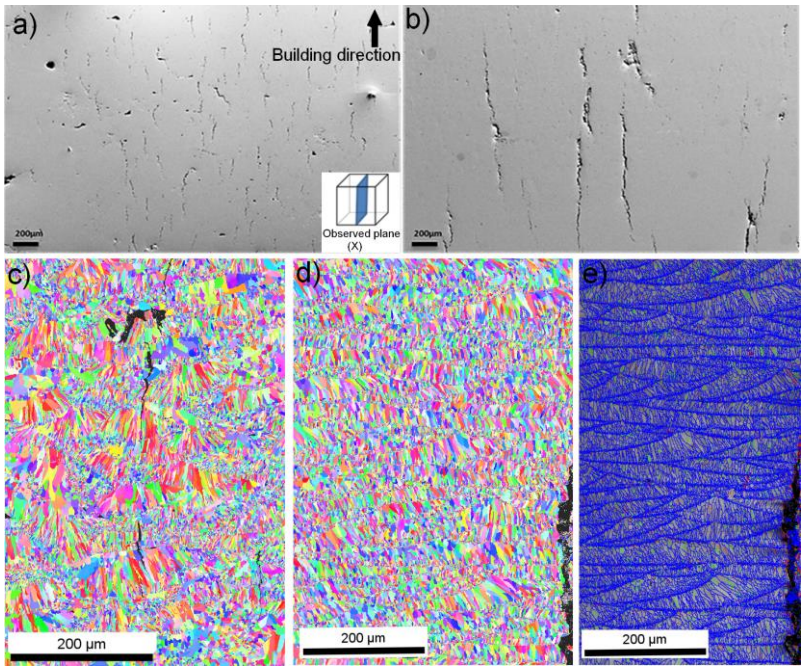

Figure 3. a, b) SEM images of S1 and S2 respectively; c) and d) represent the inverse pole figure (IPF) of S1 and S2; e) shows the high (blue colored) and low (green and red-colored) angle grain boundaries of the S2 sample.

EBSD analyses were done on the X-plane to observe the melt pool shape resulting from the L-PBF process. The melt pool is effectively observable through the convex structure following the build direction. Elongated grains following the build direction are observed in line with the typical L-PBF microstructure (Figure 3e). For both materials (S1 and S2), smaller grains are present at the junction of melt pools. This phenomenon can be explained in part by the dendritic structure present at the melt-pool junction (Figure 4a) and which is a favorable nucleation site [7]. To investigate the origin of cracks, we performed EDX analysis on the S1 sample (Figure 4), which shows small elemental segregation. Indeed, Zr and Ti elements seem to be enriched in the inter-dendritic region. In contrast, Ta is present mainly in the dendrite. However, this is not enough evidence for the moment to relate it to crack initiations. Additional work is needed.

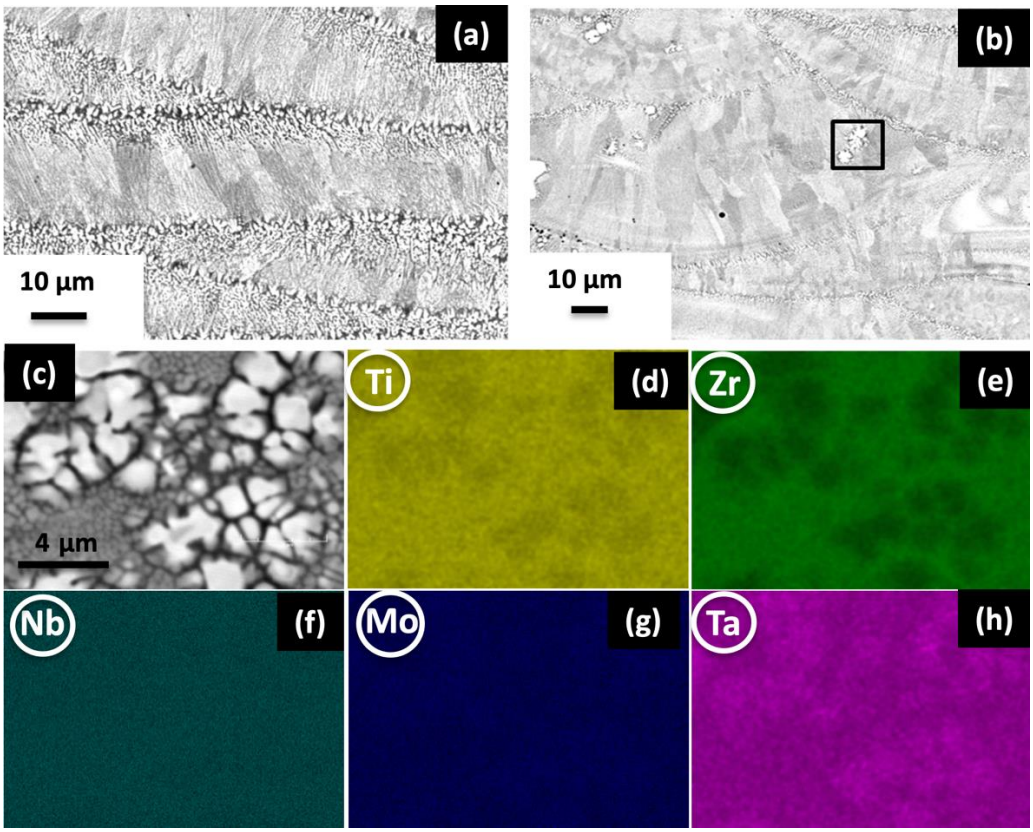

Figure 4. a-b) shows the microstructure of the S1 sample using backscattered electrons, c) is an enlargement over b); d-h) represents EDX mapping performed on c)

Preliminary compression test results are shown in Figure 5. The tests were conducted at room temperature. While the S2 sample has broken prematurely due to numerous macrocracks (see Figure 3c), the mechanical properties of the S1 sample could be investigated. Overall, the compression behavior is direction-dependent. The yield strength and ultimate compression strength (1450 MPa and 1800 MPa, respectively) in the built direction are higher than in the X direction (1250 MPa and 1750 MPa, respectively). The plastic deformation follows a similar trend, as about 10 % and 5 % of plastic deformation have been found for the Z and X-direction, respectively. These results are better than those estimated with rules of mixtures [15,16] and can still be enhanced with further microstructure optimization via parameter adjustments and or post-treatment by hot isostatic pressing. Finally, the mechanical behavior seems to be strain-rate independent, as the strain-stress curves superimposed on each other in the range 10^{-4} s^{-1} to $10^{-2}s^{-1}$. Notice that tensile yield stress at 0.2 % offset of about 1690 MPa has been reported by Nakano et *al.*[7].

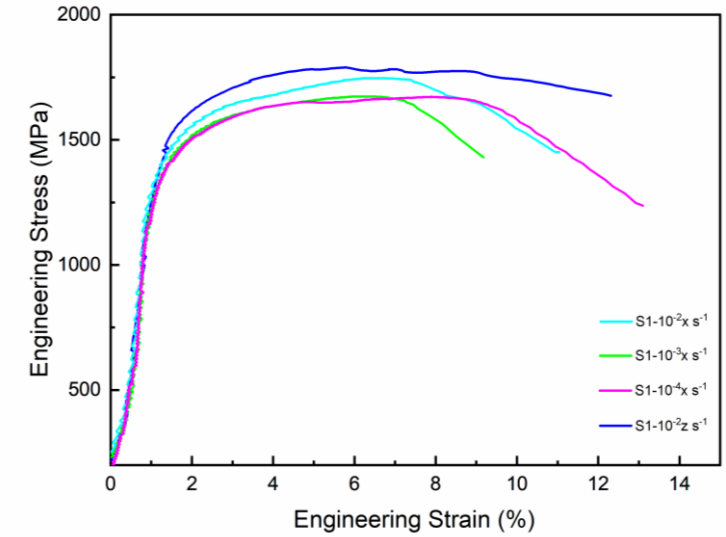

Figure 5. Engineering stress–strain response of the sample S1 during room temperature compression tests illustrating the effect of the strain rate and of the orientation of the compression axis.

Machinability and the influence of the milling parameters on the roughness
After milling, surface topography is recorded, and six roughness parameters are measured and analyzed for each surface. Each milled surface was optically recorded (Figure 6)

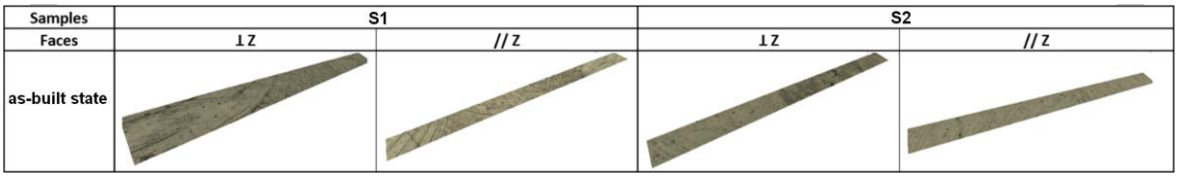

Figure 6. Milled surfaces recordings

The observations of the milled surfaces reveal anisotropic topography with peaks and valleys, whatever the tool diameter and the material. Ridges (cycloids) left by tool teeth can be seen on all the milled surfaces. Each milled surface topography was optically recorded (Figure 7).

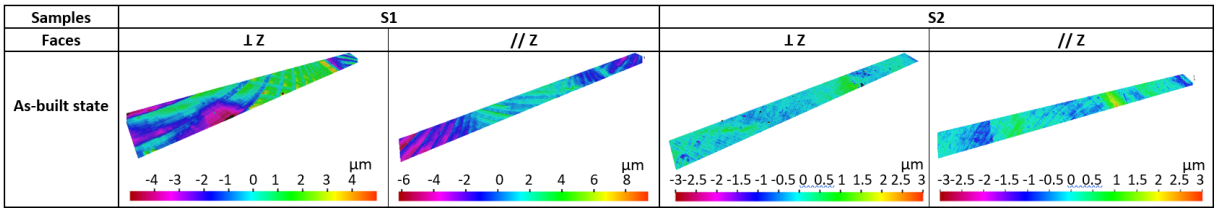

Figure 7. Milled surfaces topography

Cycloids left by tool teeth can also be seen on the milled anisotropic surfaces' topographies. No significant differences can be seen between S1 samples (milled with a 6 mm diameter tool) and S2 samples (milled with an 8 mm diameter tool).
The surface roughness parameters of the four samples were measured. The two surfaces of each sample were analyzed. The roughness results are reported in Table 3.

Table 3. Roughness parameters results

Roughness	Materials	as-built state			
	Samples	S1		S2	
	Faces	⊥ Z	// Z	⊥ Z	// Z
Settings	Lc (µm)	800	800	800	800
	Measured width (mm)	2.131	1.782	1.573	1.829
	Measured height (µm)	311.114	321.775	316.788	305.599
	2D profile length (mm)	4.374	4.36	4.36	4.376
2D	Ra (µm)	0.6	0.555	0.142	0.246
	Rt (µm)	5.104	4.333	1.338	2.548
	Rz (µm)	3.137	3.224	0.996	1.744
3D	Sa (µm)	0.663	0.515	0.515	0.224
	Sz (µm)	16.191	10.095	5.305	4.735
	Sdr %	0.497	0.453	0.187	0271

Ra and Sa roughness values are all above 1 micron. Alla et al. [17] noted the same range of Ra values (0.3 to 0.6 µm) when machining implants. About the abutment part, a smooth or even polished surface abutment was considered the most appropriate at this level. However, a rough surface is acceptable as no link to periodontal tissue response has been demonstrated [18]. About the body part, the original Brånemark implant (Nobel Biocare) owned a surface roughness between 0.5 and 1.0 µm in Sa value. Berenguer et al. studied the roughness of marketed titanium dental implants, for which the body areas had a mean Sa value of 0.76 ± 0.08 µm [19]. However, implants of a Sa roughness of about 1.5 µm show a stronger bone response. [20]. Our values are relatively good when a milling process is used in metallic materials. According to the literature, higher values would also have been acceptable in these conditions. All the six roughness parameters values are higher when the 6 mm diameter tool is used, whatever the sample and the face orientation regarding the building direction. This is consistent with the fact that a larger tool diameter provides a smoother surface. Rt, Rz, and Sz values are higher than Ra and Sa values, whatever the sample, the tool diameter, and the face orientation regarding the building direction. The Ra and Sa parameters are based on an arithmetic mean, so extreme points have a limited influence on Ra and Sa. Rt, Rz, and Sz are extremum parameters. Due to the intrinsic definition of these roughness parameters, giving much weight to the maximum points, Rt, Rz, and Sz are more sensitive to extreme points. Ra and Sa (average parameters) values on the milled surfaces perpendicularly to the Z-building direction are slightly higher. Rt, Rz, and Sz (extremum parameters) values are almost the same, whatever the face orientation regarding the building direction. The hybrid parameter Sdr values are higher on the milled surfaces parallel to the Z-building direction. This is consistent with the increase of the developed surface induced by the 3D printing slices. The other roughness parameters do not highlight this point.

Conclusions

In this study, $Ti_{1.4}NbZrMo_{0.3}Ta_{0.3}$ RHEA has been processed by L-PBF. This preliminary work aims to obtain a solid bulk solution with adapted microstructure and mechanical properties for bio-implants. Two sets of L-PBF parameters have been studied; both presented different default patterns but identical microstructures typical of L-PBF materials. In terms of mechanical property, quasi-static room temperature compression tests indicate high yield strength and ultimate compression strength along with a good plasticity in the range 5-10 %, which are acceptable for the intended application despite the presence of cracks that could be leveled off by adjusting L-PBF process parameters combined with post-treatment sequences. It is interesting to note that while the mechanical behavior of the as-built parts is dependent on the loading direction (X or Z), no strain-rate effect on the mechanical properties is observed in this work. The roughness parameter values agree with those found on other metallic materials. These innovating materials' machinability is correct. Low roughness parameters were measured, but the low machining speeds and a relatively high-milling time were observed. Further experiments must be carried out to decrease machining time and optimize machining parameters while sustaining roughness values in line with the expected surface functionalities.

Bibliography

[1] B. Cantor, Microstructural development in equiatomic multicomponent alloys, Mater. Sci. Eng. A. (2004) 6.

[2] J.-W. Yeh, S.-K. Chen, S.-J. Lin, J.-Y. Gan, T.-S. Chin, T.-T. Shun, C.-H. Tsau, S.-Y. Chang, Nanostructured High-Entropy Alloys with Multiple Principal Elements: Novel Alloy Design Concepts and Outcomes, Adv. Eng. Mater. (2004) 5.

[3] M. Laurent-Brocq, A. Akhatova, L. Perrière, S. Chebini, X. Sauvage, E. Leroy, Y. Champion, Insights into the phase diagram of the CrMnFeCoNi high entropy alloy, Acta Mater. 88 (2015) 355–365. https://doi.org/10.1016/j.actamat.2015.01.068.

[4] O.N. Senkov, J.M. Scott, S.V. Senkova, D.B. Miracle, C.F. Woodward, Microstructure and room temperature properties of a high-entropy TaNbHfZrTi alloy, J. Alloys Compd. 509 (2011) 6043–6048. https://doi.org/10.1016/j.jallcom.2011.02.171.

[5] W. Ji, W. Wang, H. Wang, J. Zhang, Y. Wang, F. Zhang, Z. Fu, Alloying behavior and novel properties of CoCrFeNiMn high-entropy alloy fabricated by mechanical alloying and spark plasma sintering, Intermetallics. 56 (2015) 24–27. https://doi.org/10.1016/j.intermet.2014.08.008.

[6] D. Herzog, Additive manufacturing of metals, Acta Mater. (2016) 22.

[7] T. Ishimoto, R. Ozasa, K. Nakano, M. Weinmann, C. Schnitter, M. Stenzel, A. Matsugaki, T. Nagase, T. Matsuzaka, M. Todai, H.S. Kim, T. Nakano, Development of TiNbTaZrMo bio-high entropy alloy (BioHEA) super-solid solution by selective laser melting, and its improved mechanical property and biocompatibility, Scr. Mater. 194 (2021) 113658. https://doi.org/10.1016/j.scriptamat.2020.113658.

[8] H. Dobbelstein, E.L. Gurevich, E.P. George, A. Ostendorf, G. Laplanche, Laser metal deposition of a refractory TiZrNbHfTa high-entropy alloy, Addit. Manuf. 24 (2018) 386–390. https://doi.org/10.1016/j.addma.2018.10.008.

[9] S.P. Leo Kumar, D. Avinash, Investigations on achievable surface quality in milling of Ti-35Nb-7Zr-5Ta alloy, Mater. Manuf. Process. 36 (2021) 1800–1806. https://doi.org/10.1080/10426914.2021.1948054.

[10] S.P. Leo Kumar, D. Avinash, Influence of cutting conditions on surface characteristics in micro-milling of Ti-6Al-7Nb alloy, Mater. Manuf. Process. 34 (2019) 1783–1791. https://doi.org/10.1080/10426914.2019.1669803.

[11] R. Danzl, F. Helmli, S. Scherer, Focus Variation - a New Technology for High Resolution Optical 3D Surface Metrology, (n.d.) 11.

[12] S. Scherer, D.S. Scherer, Focus Variation – A New Technology for High Resolution Optical 3D Surface Metrology, (n.d.) 2.

[13] A. Hattal, T. Chauveau, M. Djemai, J.J. Fouchet, B. Bacroix, G. Dirras, Effect of nano-yttria stabilized zirconia addition on the microstructure and mechanical properties of Ti6Al4V parts manufactured by selective laser melting, Mater. Des. 180 (2019) 107909. https://doi.org/10.1016/j.matdes.2019.107909.

[14] L. Guo, J. Gu, B. Gan, S. Ni, Z. Bi, Z. Wang, M. Song, Effects of elemental segregation and scanning strategy on the mechanical properties and hot cracking of a selective laser melted FeCoCrNiMn-(N,Si) high entropy alloy, J. Alloys Compd. 865 (2021) 158892. https://doi.org/10.1016/j.jallcom.2021.158892.

[15] S.M. Shaikh, V.S. Hariharan, S.K. Yadav, B.S. Murty, CALPHAD and rule-of-mixtures: A comparative study for refractory high entropy alloys, Intermetallics. 127 (2020) 106926. https://doi.org/10.1016/j.intermet.2020.106926.

[16] A. Shafiei, Simple approach to model the strength of solid-solution high entropy alloys in Co-Cr-Fe-Mn-Ni system, (2020).

[17] R.K Alla, K.Ginjupalli, N. Upadhya, M. Shammas, R.K. Ravi, R. Sekhar, Surface roughness of implants: a review. Trends in Biomaterials and Artificial Organs, (2011) 25(3), 112-118.

[18] https://www.3dcelo.com/morphologie-implantaire-et-criteres-de-selection/ (June 2022)

[19] X. Costa-Berenguer, et al. "Effect of implantoplasty on fracture resistance and surface roughness of standard diameter dental implants." Clinical oral implants research (2018) 29.1 46-54.

[20] T. Albrektsson, A. Wennerberg, Oral implant surfaces: Part 1-review focusing on topographic and chemical properties of different surfaces and in vivo responses to them. International Journal of Prosthodontics, (2004) 17(5);